Journal of the Meteorological Society of Japan, Vol. 87A, pp. 255–263, 2009
DOI:10.2151/jmsj.87A.255

Use of the TRMM-PR for Estimating the TMI Beam Filling Correction

Thomas T. WILHEIT

Department of Atmospheric Science, Texas A&M University, College Station, Texas, USA

and

Christian D. KUMMEROW

Department of Atmospheric Science, Colorado State University, Fort Collins, Colorado, USA

(Manuscript received 11 July 2008, in final form 3 December 2008)

Abstract

The unresolved rainfall structure within the Field of View (FOV) of a microwave radiometer, such as TRMM Microwave Imager (TMI), causes errors in the rainfall estimation due to the nonlinear relationship between the rain rate and brightness temperature. We have used rainfall structure data from the TRMM Precipitation Radar (PR) to estimate the bias caused by this structure, the random (FOV-to-FOV) error, and a rough estimate of the regional/seasonal scale uncertainty in the bias. We have expressed this bias in terms of a rainfall variance, V, over the FOV in the form: $V = a \langle r \rangle^b$ where $\langle r \rangle$ is the FOV average rain rate in mm h^{-1}. The data were best fit by $a = 0.144\ mm^2\ h^{-2}$ and $b = 2.46$ at the pre-boost 19.35 GHz resolution. The beam filling error is very small relative to the rain rate at small rain rates but increases with increasing rain rate.

1. Introduction

In addition to its obvious use for measurement of rainfall, the Precipitation Radar (PR) is also quite useful for the determination of precipitation physics for the improvement of passive microwave algorithms The knowledge obtained from the radar can then be applied to the interpretation of the TRMM Microwave Imager (TMI) over its wider swath, and for that matter, for the interpretation of microwave radiometers flying on other satellites including those from before the TRMM launch and those in orbit after the eventual demise of TRMM. An example of this application was given by Wilheit et al. (2007) who used radar data to infer drop size distributions for inclusion in radiometric algorithms. Here we provide another example; we have used the three dimensional rainfall structure information derived from PR for better understanding of passive microwave retrievals and their uncertainties.

It is convenient to consider this structural information in two parts. First in the vertical dimension, we are interested in the surface rainfall, but the radiometric signal is, to first approximation, an integral over the entire profile and therefore provides information on the average rain rate over the liquid portion of the rain column. Thus, there is some error in expressing the radiometer-based rain rate in terms of a surface rain rate. This source of error would remain even in the limit of very high spatial resolution observations. We will leave this error for a future analysis.

Second, we can consider the (quasi-horizontal) rain fall structure perpendicular to the view direction. In Fig. 1 the solid line shows the relationship between the brightness temperature and rain rate for the 10 GHz, vertically polarized channel for a 4 km freezing level over ocean as computed with a plane-parallel model. One can see that the relationship is quite non-

Corresponding author: Thomas T. Wilheit, Department of Atmospheric Science Texas A&M University, TAMU 3150, College Station, TX 77843-3150, USA
E-mail: Wilheit@tamu.edu

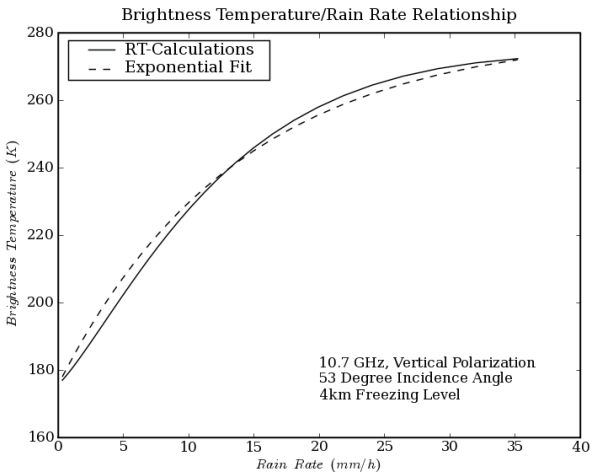

Fig. 1. Brightness Temperature as a function of rain rate computed for the 10.7 V channel of TMI assuming a 4 km freezing level (solid line). The dashed line represents the exponential approximation as used in Wang (1996).

linear and is mostly concave downwards. On the other hand, rainfall is always quite inhomogeneous over typical passive microwave FOVs. The antenna pattern can only average the brightness temperature linearly. To the extent this relationship is concave downwards, it produces an underestimate of the average rain over the FOV when a plane-parallel model is used as the basis for interpretation. This under(or over) estimate is called the Beam Filling Error (BFE) and a correction for it, the Beam Filling Correction (BFC) It must be noted at the outset that rainfall is highly structured and can only be described in approximate terms. There, inevitably, will be much scatter in our results.

Our objective, in this paper, is to understand the BFC implicit in the TRMM 2A12 algorithm and to improve the BFC in TRMM 3A11 (Wilheit et al. 1991; and Chang et al. 1993) and similar algorithms. To this end we will discuss a simulation experiment based on TRMM PR data designed to isolate the BFE. We will compute brightness temperatures Tbs for six TMI frequency/polarization pairs (10.7 V/H, 19.35 V/H, and 37 V/H). The radiative transfer computations will be performed with the full structure as observed by the PR and then with the structure smoothed to the TMI resolution. The difference between the two computations is the BFE for each member of the ensemble of PR profiles. We then develop an approximate theory to explain the difference between the two cases. Each separate frequency/polarization combination is a different probe of the ensemble of profiles, each interacting with the distribution of rainfall intensities differently. Here we have treated all frequencies as having the same resolution (that of 19.35 GHz before the orbit boost) so not to confound frequency/polarization effects with resolution effects. Since the 3A11 algorithm only uses the 19.35 V and 21.3 V channels this is almost sufficient; we still need values for the post-boost resolution. For sake of the post boost 3A11 application, for use on other instruments and even for improved understanding of the 2A11 algorithm, an obvious follow-on is to treat the resolution effects. Since even a coarse estimate of the resolution effect is useful, we have used an indirect method of deriving it. An example of the usefulness of such an estimate is establishing a mission lifetime orbital altitude decay specification for the Global Precipitation Mission Constellation Satellite.

The radiative transfer computations are based on Kummerow et al. (2006) who discussed their shortcomings. Since we are using the same radiative transfer computations both with the full structure and the smoothed structure, these shortcomings should nearly cancel. The ice phase assumptions are particularly arbitrary. Thus, we have avoided using the frequency (85.5 GHz) that would be most sensitive to this problem; the frequencies used here should be minimally sensitive to the ice phase. In any case, it will be seen that scatter in our results is large compared to any realistic radiative transfer shortcoming so the limitations of the radiative transfer model should not be a factor in our conclusions.

It would be possible to use the PR derived structure directly to correct the radiometric results explicitly for each pixel near the center of the PR swath. This would only work for a fraction of the TMI observations and not be transferrable to other microwave radiometers. Also, the use of the scattering signal in the 85.5 GHz channel for structural information has been explored (Kummerow and Giglio 1994; Aonashi and Liu 2000). This approach depends on a relationship between the ice aloft and the raindrops below that isn't unique. Moreover, in the case of TMI, there are scan-to-scan gaps between the 85.5 GHz FOVs resulting in incomplete coverage over the lower frequency FOVs. Therefore, we have used our simulations at all 3 frequencies to derive a rainfall variance model that can then be used over the entire TMI swath and for other microwave radiometers as well.

2. Background

The BFE may be understood by considering a simple model. The desired quantity is generally the average rain rate over the FOV, $\langle r \rangle$, If we express the brightness temperature observed by the satellite as an expansion of the rain rate over the FOV as:

$$\langle T_B \rangle = T_B^M(\langle r \rangle) + \frac{\partial T_B^M(r)}{\partial r}\left\langle r - \langle r \rangle \right\rangle + \frac{1}{2}\frac{\partial^2 T_B^M}{\partial r^2}\left\langle (r - \langle r \rangle)^2 \right\rangle + \ldots . \quad (1)$$

Where T_B is the brightness temperature and r is the rain rate at any particular point in the FOV. The triangular brackets, $\langle\ \rangle$, denote averaging over the FOV and the superscript M, a modeled quantity.

Ignoring terms higher than second order, the inhomogeniety over the FOV introduces a change in the observed brightness temperature:

$$\Delta T_B \cong \frac{1}{2}\frac{\delta^2 T_B}{\delta r^2} V, \quad (2)$$

Where V is the variance of the rain rate, $\left\langle (r - \langle r \rangle)^2 \right\rangle$, over the FOV. Thus, if $T_B^M(r)$ is concave downwards, as is the most common case, The brightness temperature will be less than would be expected for the average rain rate, $\langle r \rangle$. If uncorrected, this would lead to an underestimate of the mean rain rate. In Fig. 2, we show the second derivative of Eq. (2) computed for the 10.7 V channel of TMI for a 4 km freezing level. Note that the second derivative is in fact negative (concave downwards) for rain rates above 5 mm h^{-1} but is positive for lower rain rates. This same behavior is noted to a lesser degree at 19.35 GHz. At 37 GHz the second derivative never quite becomes positive at low rain rates, but the magnitude becomes very small.

There are two approaches to correcting for the BFE. In TRMM algorithm 2A12, the brightness temperatures are calculated from a high resolution database and then averaged over the resolutions of the various channels. These theoretical TBs are then used for interpreting the observed TBs. Thus, the BFC is implicit. Nevertheless, the results of this paper provide insight into the inner workings of the 2A12 algorithm and one potential impact of the use of an inappropriate database. Although the database used in this study contains a high degree of spatial structure, the radiative transfer calculations both for this study and for the 2A12 algorithm are performed in a modified plane parallel manner (discussed later). While it would seem desirable to perform the radiative transfer calculations using a three dimensional code, these approaches are extremely computer time intensive and would not be practical for a database large enough to support a reasonable algorithm.

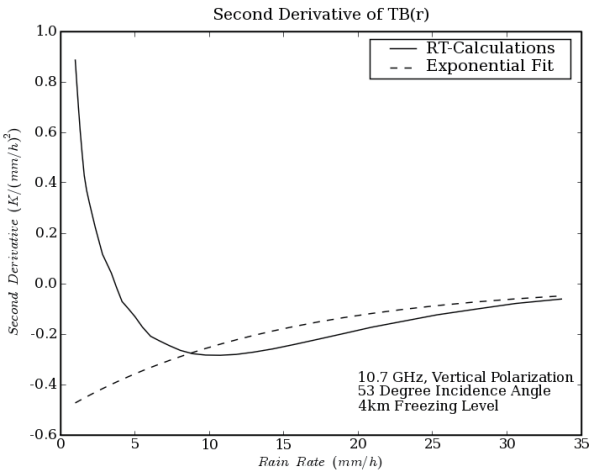

Fig. 2. Second derivative of the Brightness Temperature with respect to rain rate computed from the 10.7 V Brightness Temperatures shown in Fig. 1 (solid line). The dashed line represents the corresponding second derivative based on the exponential approximation as used in Wang (1996).

On the other hand, TRMM algorithm 3A11 uses TBs computed from a plane parallel radiative transfer model and then applies a BFC to the retrieved average monthly rain rates. In particular, it uses the correction derived by Wang (1996), based on airborne radar data from TOGA/COARE. He used these radar data to drive a simulation model that treated the RR-TB relationship as a simple exponential of the form:

$$T_B = T_0 + (280K - T_0)(1 - \exp(-r/r_c)), \quad (3)$$

where: T_0 is the brightness temperature in the absence of rain. He termed r_c "characteristic rain rate" and it is determined by the frequency, view angle, polarization and freezing level. He approximated the effect of integration along the view path by using the

rain rate averaged along the view path from the freezing level, reflected off the ocean surface and back to the freezing level. This so-called "slant path approximation" introduces a scale length of roughly twice the freezing level into the radiative transfer. To the extent that the absorption coefficient of the rain is linear in rain rate, this is a reasonable approximation. The linearity is much better at 19 and 37 GHz than at 10 GHz. He computed a simple multiplicative BFC of the form:

$$\langle r \rangle_{true} = C \langle r \rangle_{retrieved} . \quad (4)$$

According to Wang's simulation study, C could be expressed in terms of r_c and L, the long dimension of the FOV in km as:

$$C = 1 + (0.478\, Log(L) - 0.687) / r_c . \quad (5)$$

The freezing level and viewing parameter dependences are embedded in r_c. Note that C becomes 1 at a spatial resolution of 4.2 km, reflecting the spatial scale introduced by the slant path approximation. Obviously this relationship would not be valid for resolutions less than 4.2 km and would be quite doubtful near this value. The relevant TMI channels (10.7 to 37 GHz) have resolutions much larger than this limit. The data available were not sufficient to contradict the simple multiplicative form. The much greater volume of PR data enables us to examine this question in more detail.

In Fig. 1, the dashed line shows an exponential fit of the form of Eq. (3) to the 10 V (4 km freezing level) computations. While generally consistent, there are significant departures. On the other hand, in Fig. 2 the dashed line indicates the corresponding second derivative; here the behavior is markedly different at low rain rates. Although the fit is significantly better for 19 and 37 GHz, this must be considered a serious deficiency of the Wang (1996) approach.

3. Data

The data used are the PR derived rain rates for 1998. The computations are discussed in depth by Kummerow et al. (2006). For the near-nadir radar pixels corresponding to the 51st and 54th TMI pixel positions, the rain rate below the freezing level and the snow density above inferred from the radar are integrated to produce brightness temperatures. The view path integral is explicitly included for the emission portion of the computation to the extent permitted by the 4 km resolution of the PR, but the diffuse radiation is still treated as plane-parallel. This approximation was examined by Roberti et al. (1994) using three dimensional computations and found to be reasonable as long as absorption is the dominant process as is the case for the frequencies discussed in this paper. The approximation is much worse for situations where scattering dominates. The use of this ray-tracing approximation improves on the slant path approximation of Wang (1996) in that it is no longer necessary to approximate the absorption coefficient as linear in the rain rate. For this work, the Kummerow et al. (2006) computations were expanded to include the 10 and 37 GHz channels in addition to the 19 GHz, albeit at the 19 GHz (pre-orbit-boost) spatial resolution.

The TBs can be transformed from the PR resolution the radiometer resolution in two ways. The TBs can be calculated at the full resolution and then smoothed. This is essentially what the radiometer antenna pattern does. Alternatively, the rain fields can be smoothed to the radiometric resolution and then the radiative transfer calculations performed to produce TBs at the lower resolution. This latter way is implicit in the 3A11 algorithm. The difference between the two is the BFE. The 1998 data set was processed in both ways to examine this effect. The resulting data were binned by freezing level in 100 m increments. The radar profiles were summarized as a surface rain rate and a mean vertical slope which were converted into a mean rain rate from the surface to the freezing level. The brightness temperatures were then binned in increments of 10% in column mean rain rate.

4. Analysis

Figure 3 shows the standard deviations in the bins described above of the brightness temperature difference, ΔT, as a function of FOV and column mean rain rate, <r>. This primarily reflects the FOV-to-FOV variability of the effect of inhomogeniety, i.e., the random component of the BFE. Even if an algorithm has an implicit BFC, this random error will remain. Note that it is generally larger than typical instrument noise ($NE\Delta T$) values by as much as an order of magnitude. The statistical behavior of the error would differ from $NE\Delta T$ in that the errors would be highly correlated between the two polarizations at a given frequency. The random error increases as a function of rain rate roughly as $<r>^{0.4}$ until saturation effects become important as seen in the 37 GHz data. The values, to first order, reflect the variations of sensitivity of each

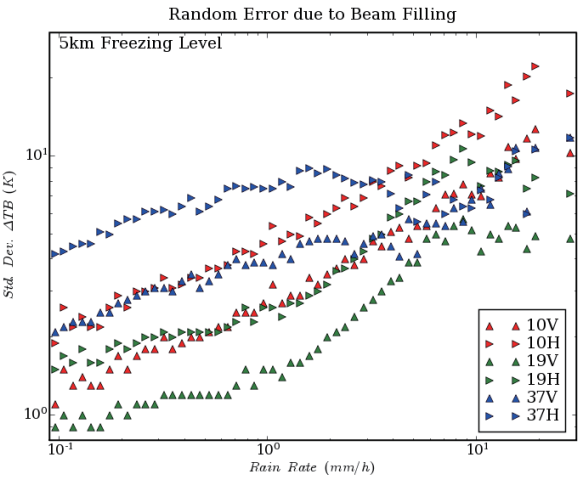

Fig. 3. Estimate of the random (FOV-to-FOV) variability of the effect of rainfall inhomogeniety in the relevant TMI channels for a 5 km freezing level.

channel to rain rate. This sensitivity increases with frequency and the horizontal polarization is more sensitive than the vertical polarization because of the surface emissivity difference.

Equation (2) can be used to interpret the mean values of ΔT. We have binned the calculations as described above and have examined the data for 2, 3, 4 and 5 km freezing levels. The variance, V, is assumed to be related to the rain rate as:

$$V = a\langle r \rangle^{b}. \tag{6}$$

We fit the values of a and b to minimize the RMS difference between the ΔTs from Eq. (2) and the simulations using all 6 frequency/polarization combinations and freezing levels of 2, 3, 4, and 5 km. The values of a and b were adjusted to minimize the rms difference between the ΔTbs from the simulations

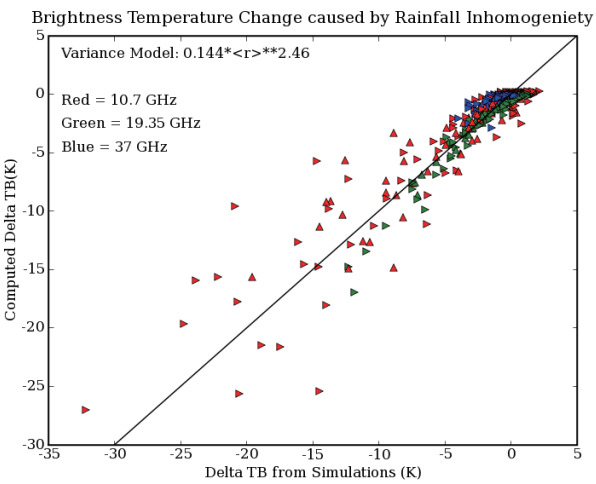

Fig. 4. Comparison of the change in brightness temperature derived from simulations and computed from a rain rate variance model. The quantities are averages over many cases binned by freezing level and rain rate. The results are given for both polarizations at 10, 19 and 37 GHz. The color indicates frequency and the upward pointing triangles indicate vertical polarization and the right pointing triangles, horizontal. The diagonal black line indicates a 1:1 relationship.

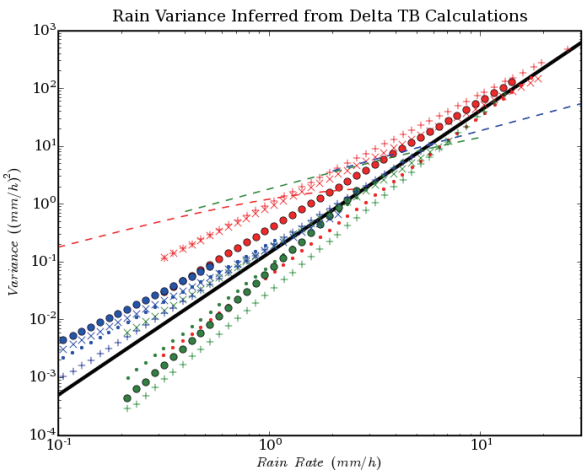

Fig. 5. Best fit variance models for individual frequencies and freezing levels. The colors of the symbols and lines denote the frequency (Red = 10.7 GHz, Green = 19.35 GHz, Blue = 37 GHz) and the shape and size of the symbol denote the freezing level (+ = 2 km, x = 3 km, small dot = 4 km, large dot = 5 km). The results for the two polarizations at each frequency and freezing level differ only slightly and have been combined for graphical clarity. The variance model implied by the Wang BFC is also shown for characteristic rain rates of 1(Red), 4 (Green) and 20 (Blue) mm h^{-1} as dashed lines. The heavy black line represents the overall best fit variance model, $V = 0.144\langle r \rangle^{2.46}$.

and from Eq. (2). The best fit was for $V(mm^2\ h^{-2}) = 0.144 < r(mm\ h^{-1}) >^{2.46}$. The value of b is intuitively satisfying; if all rain rates were equally structured in a logarithmic sense, the value of b would be 2. That it is slightly larger says that heavy rains are somewhat more structured than light rains. The variance would depend on the size of the FOV; in these computations, the size is that of the 19 GHz channels of TMI before the orbit boost (i.e., 18 km x 30 km). Figure 4 shows the comparison between the ΔTs from simulation and modeling. There is certainly some scatter but the overall trend is reproduced. The larger absolute value ΔTs reflect only a few tens of observations so a significant residual of the random error shown in Fig. 3 remains. On the other hand, there are coherent discrepancies at low rain rates (the upper right corner of the figure.) These reflect the shortcomings of the expansion about a point of Eq. (2). The second derivative in Eq. (2) has a low absolute value and, in some cases is even positive, but for typical FOVs there will be some fractional coverage of significantly higher rain rates for which the second derivative is much different than at the FOV mean rain rate.

Estimating the random component of the BFE is straightforward as discussed earlier. However, an estimate of any consistent biases in the BFC that may depend on rain rate or freezing level is much more difficult. This error will survive as a global, regional or seasonal bias in spite of averaging a great many observations. To approximate this uncertainty, we have performed the fit separately for each freezing level, polarization and frequency in our data. These fits are shown in Fig. 5. The variability of V from one fit to another is very large at low rain rates but becomes smaller near and above 10 mm h^{-1}. The fits are displayed by color for frequency and character for freezing level. The results for the two polarizations differ only slightly and have been combined in the figure to reduce clutter. The data shown and used are restricted to the range of rain rates for which a given channel is useful. At low frequencies (and to a lesser degree low freezing levels) there is no useful sensitivity at very low rain rates. On the other hand, at high rain rates the sensitivity to rain rate also decreases due to saturation particularly at high frequencies and high freezing levels. No clear dependence on frequency or freezing level emerges from the data. In order to estimate the ratio by which the variance model is uncertain, the logarithm of the ratio of the variance of each (Frequency/Polarization/Freezing Level) fit to the variance given by the overall best fit (i.e., $V(mm^2\ h^{-2}) = 0.144 * < r(mm\ h^{-1}) >^{2.46}$) was computed for a sequence of rain rates as shown in Table 1; the standard deviations of these values (converted back to ratios) are also given in Table 1. Since Fig. 5 is a log-log plot, these ratios are proportional to the vertical distance between each variance model and the best fit variance model (shown as the heavy black line). Note that the uncertainty is more than a factor of 4 near 0.1 mm h^{-1} but decreases to a factor of 1.29 at higher rain rates. This underscores the difficulty of quantifying the BFC and its associated uncertainty.

It is straightforward to invert the Wang BFC to retrieve the implied variance model based on Eqs. (2) and (3) For r_c values of 1, 4 and 20 mm h^{-1} this retrieval is also included in Fig. 5. (These values correspond roughly to 37 GHz/5 km freezing level, 19 GHz/4.5 km and 10.7 GHz/3.5 km respectively.) The agreement with the present work over the range of a few mm h^{-1} is quite reasonable but at low rain rates (< 1 mm h^{-1}) the Wang BFC significantly overcorrects the rain rate and undercorrects at high rain rates. Figure 6 also shows the overall best fit (dashed line) and the + and – 1 σ values by the upward and downward pointing triangles. For reference, the variance implied by the Wang BFC is also shown for the same 3 values of r_c .

Since all these computations were done for the 19.35 GHz (pre-boost) resolution, and repeating them

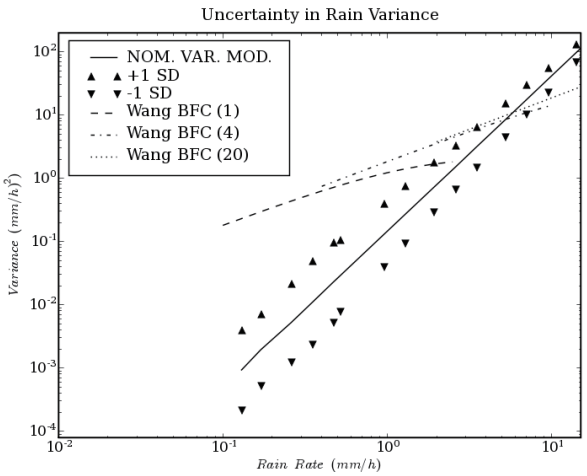

Fig. 6. The uncertainty in the variance model. The black line indicates the overall best fit variance model ($V = 0.144 < r >^{2.46}$), the upward pointing triangles the best fit $+1\sigma$ and the downward pointing triangles, -1σ. For reference the variance implied by the Wang BFC is also shown for r_c values of 4 and 20 mm h^{-1}.

Table 1. Correlated Error Estimates.

Rain Rate (mm/h)	.13	.17	.26	.35	.47	.52	.95	1.3	1.9	2.6	3.5	5.2	7.0	9.5	14	17
Uncertainty In Variance	4.3	3.7	4.2	4.6	4.3	3.6	3.2	2.8	2.5	2.2	2.1	1.9	1.7	1.6	1.4	1.3

The variance model fits were performed for each frequency/polarization/freezing level combination separately. For the sequence of rain rates indicated above, the standard deviations (in a logarithmic sense) of the variance models from the overall best fit variance model were calculated. These rms deviations (converted back to ratios) are then the estimates of the systematic uncertainty of the best fit variance model

for other resolutions is computationally very intensive, the question remains of how to adjust the results for different resolutions. We can use the Wang BFC for some insight, but hardly a solution. We have solved for the variance implied by various resolutions ranging from 15 to 70 km for rain rates in the range 3.3 to 7.4 mm h^{-1}, the range for which the Wang results are within the $\pm 1\sigma$ of the present best fit variance model. The computations were performed for r_c values of 4 and 20 mm h^{-1}, the rain rates are too large for the r_c value of 1 mm h^{-1} to be reasonable. The variances are then divided by the similarly computed variance for the 19.35 GHz resolution, 30 km. The resulting Variance Adjustment Factor (VF) is shown in Fig. 7; the Xs represent the r_c = 20 mm h^{-1} computations and the crosses(+), 4 mm h^{-1}. There is essentially no rain rate dependence noted for the larger r_c value, (The Xs appear bold because of multiple, almost coincident values being plotted.) but a great deal for the smaller r_c value. For reference we have plotted lines of:

$$VF = 1 + c \cdot \log(L/30\,km), \qquad (7)$$

where L is the long axis of the FOV in km. We have used 0.3, 0.4, and 0.5 as values of c in Fig. 7. The c value of 0.5 gives a very good fit to the r_c = *20* mm h^{-1} computations over the whole range and the r_c = *4* mm h^{-1} computation are contained between the c = *0.3* and c = *0.5* curves. Earlier it was noted that the Wang (1996) BFC became 1 at a resolution of 4.3 km; a BFC of 1 implies a zero variance. A value of c = *0.51* would be consistent with this observation. We thus have a suggestion that the variance can be scaled as in Eq. (7) above with a value of c between 0.3 and 0.5, with somewhat more support for the upper end of this range. Note that the adjustment to the variance for any TMI relevant resolution is still less than the uncertainty in the variance.

5. Conclusions

We have used a simulation study to examine the

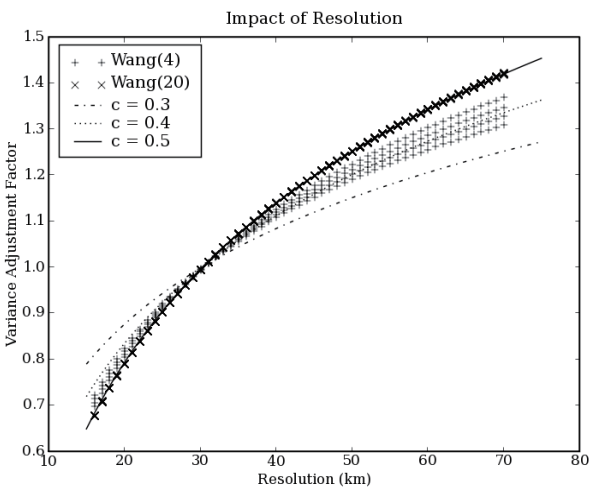

Fig. 7. VF, the ratio of the variance implied by the Wang (1996) BFC for a given resolution to that for a 30 km (TMI, 19.35 GHZ, Pre-Boost) resolution. The computations were performed for the range of rain rates (3.3 to 7.4 mm h^{-1}) where the Wang model is consistent with the present work. The Xs represent calculations for r_c = 20 mm h^{-1} and the +s for 4 mm h^{-1}. The +s nearest the c = 0.5(bold) curve are for the low end of the range (3.3 mm h^{-1}) and those farthest from the c=0.5 curve, the high end of the range (7.4 mm h^{-1}). The sensitivity to rain rate for r_c = 20 mm h^{-1} is so slight that it simply makes the Xs appear bold. Reference lines for VF = 1-c* log(Res/30 km) are shown for c = 0.3, 0.4 and 0.5. This provides an estimate of the impact of changing spatial resolution on the variance model.

BFC for TMI using data from the TRMM PR and found that, to a fair approximation, the BFC can be described by a simple variance model, admittedly with a great deal of scatter. When the data are subdivided by freezing level and by radiometer frequency, a wide variety of variance models emerge that are strikingly different at low rain rates. This scatter results from a poor signal to noise produced by small second derivatives of the TB(r) function at low rain rates and by large variations of rain rate along the view path. The impact of this large scatter is mitigated by noting first that the absolute values of the variances are very small and that the small second derivatives also imply a weak BFE. As a result, the large uncertainties at very low rain rates have little impact. This can be seen clearly in Fig. 8. Here we have computed the brightness temperature for the 19.35 V channel of TMI assuming a 4 km freezing level. Using other frequencies, polarizations or freezing levels would not lead to significantly different conclusions. The dashed line represents the calculation ignoring the BFE. Correcting it by computing the ΔTBs using Eq. (2) and the best fit variance model (a = 0.144; b = 2.46 in Eq. 6), results in the solid line. One can see that the BFC moves towards 1 in the low rain rate limit. The Wang (1966) would be a constant offset to the right in this semilog plot. The envelope of the ±1σ variances given in Table 1 is well approximated by a = 0.36; b= 2.22 (upper) and a = 0.054; b = 2.71 (lower) at least up to 17 mm h^{-1}. The use of these variance models results in the dash-dot and dotted lines respectively. If we were to observe a brightness temperature of 250 K on this channel over an atmosphere with a freezing level of 4 km and ignore the BFE, we would infer a rain rate of 3.4 mm h^{-1}. If we make a correction based on our best fit model, the inferred rain rate would increase to 3.9 mm h^{-1} for a BFC of 1.15. Using the +1σ model would increase the inferred rain rate to 4.8 mm h^{-1}, or a BFC of 1.41; -1σ yields 3.6 mm h^{-1} and a BFC of 1.09. For reference the Wang (1996) BFC for these circumstances is 1.20, well within the uncertainty limits. It is clear from this figure that the BFC is smaller at lower rain rates and larger at higher rain rates.

The variance model derived here is only valid for the 19 GHz (pre boost) TMI spatial resolution. While we have generated an approximate scaling function to allow us to predict the variances post boost and for different frequencies (and, for that matter, different instruments on different satellites), it is difficult to have much confidence in this scaling since it is based on the Wang (1996) BFC with its shortcomings.

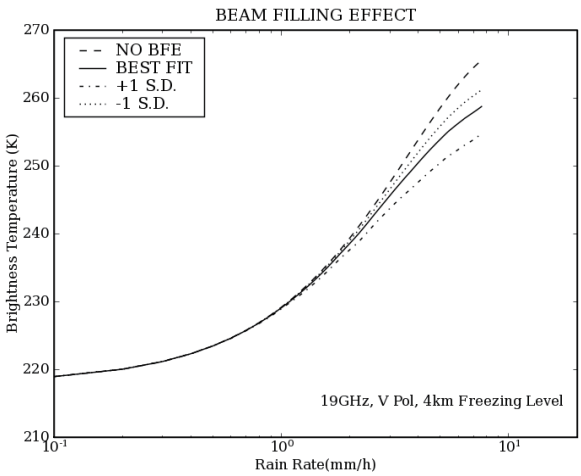

Fig. 8. Impact of the inhomogeniety of rain rate on brightness temperature for the 19 GHz, V-pol, 4 km freezing level case. The dashed line results if the inhomogeniety is ignored, the solid line if we use the best fit variance model. If we change the variance model by + or – 1σ , the dash-dot and dotted lines result respectively.

It would be straightforward to incorporate the results of this analysis into the 3A11 algorithm. The spatial resolution issue would not be a factor as all of the Tbs used in 3A11 are at (or very near) the resolu-

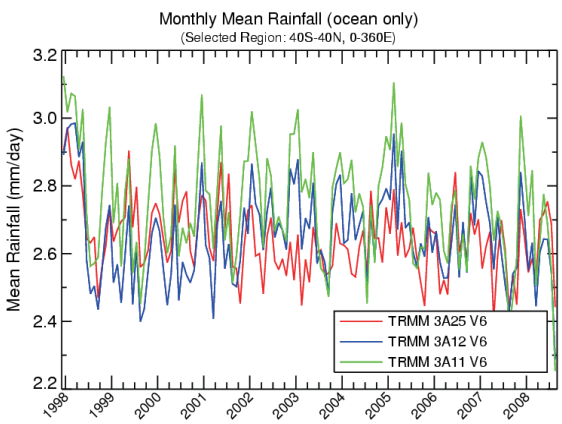

Fig. 9. Global averages of oceanic rainfall (by montsh) from the TRMM Precipitation Radar (3A25) and from two TMI algorithms, 3A25 and 3A11. 3A12 and 3A25 are monthly averages of the TRMM Level-2 standard products 2A12 and 2A25 respectively

tion used in these simulations. It was noted that the constant percentage correction currently used in 3A11 undercorrects at rain rates greater than a few mm h^{-1} and overcorrects at lower rain rates. Since the bulk of the rain contribution is from the lower rain rates the net effect should be a decrease in the retrieved rain totals. Without actually performing the calculations, it is difficult to estimate the net effect but a decrease of the order of 10% with significant regional variations would not seem unreasonable. Figure 9, extracted from http://rain.atmos.colostate.edu as discussed by Berg and Kummerow (2005), shows that the retrievals from 3A11 are consistently higher than those from 2A11 or from the PR. A decrease of the order of 10% in 3A11 would improve its agreement with the other two algorithms.

Acknowledgments

The Authors gratefully funding support from the NASA Precipitation Measurements Program.

References

Aonashi, K., and G. Liu, 2000: Passive microwave precipitation retrievals using TMI during the Baiu period of 1998. Part I: Algorithm description and validation. *J. Appl. Meteor.*, **39**, 2024–2037.

Berg, W., and C. Kummerow, 2005: The climate rainfall data center: an online data service center, *Bull. Amer. Meteor. Soc.*, **86**, 1237–1240.

Chang, A. T. C., L. S. Chiu, and T. T. Wilheit, 1993: Random errors of oceanic monthly rainfall derived from SSM/I using probability distribution functions. *Mon. Wea. Rev.*, **121**, 2351–2354.

Kummerow, C., and L. Giglio, 1994: A passive microwave technique for estimating rainfall and vertical structure information from space. Part I: Algorithm description, *J. Appl. Meteor.*, **33**, 3–18.

Kummerow, C., W. Berg, J. Thomas-Stahle, and H. Masunaga, 2006: Quantifying global uncertainties in a simple microwave rainfall algorithm, *J. Atmos. Oceanic Technol.* **23**, 23–37.

Roberti, L., J. Haferman, and C. Kummerow, 1994: Microwave radiative transfer through horizonally inhomogeneous precipitating clouds. *J. Geophys. Res.*, **99**, 16707–16718.

Wang, S. A., 1996: Modeling the beamfilling correction for microwave retrieval of oceanic rainfall, Ph.D. thesis, Department of Meteorology, Texas A&M University.

Wilheit, T. T., A. T. C. Chang, and L. S. Chiu, 1991: Retrieval of monthly rainfall indices from microwave radiometric measurements using probability distribution functions. *J. Atmos. Oceanic Technol.*, **8**, 118–136.

Wilheit, T. T., V. Chandrasekar, and W. Li, 2007: Impact of uncertainty in the drop size distribution on oceanic rainfall retrievals from passive microwave observations, *Trans IEEE, Geosci. Rem. Sens.* **45**, 3160–3164.